Angular dispersion boost of high order laser harmonics with Carbon nano-rods

ZSOLT LÉCZ[1,*] (ID) AND ALEXANDER A. ANDREEV[1,2,3]

[1] *ELI-ALPS, ELI-HU Nonprofit Ltd, Dugonics sqr. 13, Hungary*
[2] *Max-Born Institute, Berlin, Germany*
[3] *Institut fur laser und Optik, Hochschule Emden, Leer University of Applied Sciences, Emden, Germany*
[*]zsolt.lecz@eli-alps.hu

Abstract: Periodic surface gratings or photonic crystals are excellent tools for diffracting light and to collect information about the spectral intensity, if the target structure is known, or about the diffracting object, if the light source is well defined. However, this method is less effective in the case of extreme ultraviolet (XUV) light due to the high absorption coefficient of any material in this frequency range. Here we propose a nanorod array target in the plasma phase as an efficient dispersive medium for the intense XUV light which is originated from laser-plasma interactions where various high harmonic generation processes take place. The scattering process is studied with the help of particle-in-cell simulations and we show that the angular distribution of different harmonics after scattering can be perfectly described by a simple interference theory.

1. Introduction

Limited size targets exposed to intense coherent radiation constitutes a well-studied plasma phenomenon involving linearly excited surface plasmon oscillations. Such laser-matter interactions have been extensively investigated, both in metal clusters [1] and in laser-ionized rare-gas atomic clusters [2,3]. The absorption and scattering of the incident light is well described by the Mie theory, which predicts the existence of a resonance condition corresponding to the multi-pole oscillation of a portion of free electrons in the target with respect to the background of the positively charged ions. In the resonant regime, efficient excitation of plasma oscillations can result in a considerable enhancement of the cluster's inner and outer electric field at the fundamental frequency. This, in turn, may significantly enhance the scattered field intensity at large angles with respect to the original wave direction.

It is well known that intense short laser pulse can produce high harmonics during the interaction with solid density surfaces via different surface high harmonic generation processes [4]. It was shown that the efficiency of such process can be about 10^{-4} or 10^{-3}, for instance at the ninth harmonic [5,6]. It corresponds to a harmonic wave intensity on the order of $10^{14} - 10^{15}$ W/cm^2, which is already high enough to ionize a Carbon or Si nanorod, which are routinely manufactured in many laboratories [7,8]. It is possible to achieve higher charge states if the radiation reflected from the flat surface is not filtered and the fundamental frequency also interacts with the nanorods, but in this case the plasma expansion may influence the scattering and reduce the efficiency. For the present analysis we consider ionized Carbon nanorods with a charge state 4+, which corresponds to an electron density of $\approx 2.4 \times 10^{23}$ cm^{-3}, and with 200 eV electron temperature. For these parameters the electron collision rate is a little lower than the harmonic frequency and our simulations show that the interaction can be considered collision-less for the above mentioned radiation intensity.

In the case of high harmonics generated in gases the radiation intensity is at least 4 orders of magnitudes lower [9–11], which is not enough to ionize the target and to generate a plasma with purely imaginary refractive index. In this case a preceding pulse should be used which

pre-ionizes the nanorods, or one can consider unionized target which has a different refractive index [12] leading to different resonant conditions and lower scattering efficiency.

In the range of micrometer long wavelengths photonic crystals and gratings can be manufactured for guiding or diffracting the electromagnetic waves [13,14] while for x-ray radiation real crystals can be used where the scattering centers are atoms regularly placed at distances of few nanometers [15]. There is a gap between these very different wavelength regimes, which is called the XUV regime, where the manipulation of light propagation could not evolve as much as for other wavelengths. It has been shown that gas jets can serve as refractive medium for XUV pulses [16] and diffraction at such wavelength can be achieved on metal Fresnel-zone plates [17] leading to focusing of radiation with wavelength as short as 100 Å.

Within the present work we do focus on the possibility of directed scattering and angular filtering of short wavelength radiation in the XUV range by scattering on suitable nanorod arrays. The nanorods have many advantages with respect to the clusters, because the separation distance between them as well as their radius can be well controlled. The general setup of such interaction is shown in Fig. 1. The harmonics contained by the main pulse are emitted with different intensity at different angles, which results in angular dependent waveform of the outgoing radiation. The scattering by a single nanorod can be completely described in cylindrical symmetry and the interaction can be easily modeled with the help of 2D particle in cell simulations. In particular, we concentrate on a theoretical investigation, supported by simulations, and we point out the applicability for experimental realisation.
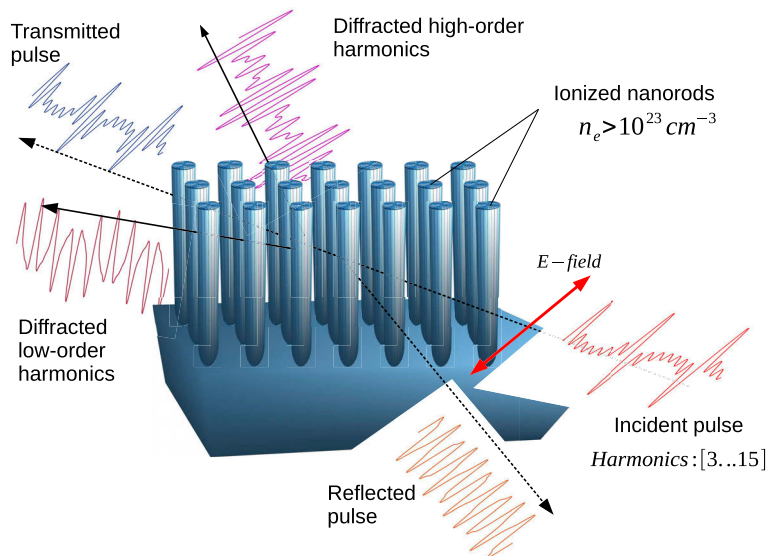
Fig. 1. The geometry of the studied interaction. The plane of polarization is perpendicular to the nanorods. The length of the nanorods is a few micrometers (longer than the attopulse spot size) and in simulations we consider only a few horizontal rows of nanorods. The waveforms of outgoing waves in different directions are shown for illustration, the angular distribution of harmonics depends on the distance between the rods.

2. Basic model estimations

Let us consider a single nanorod with radius a irradiated by a short harmonic pulse with a duration $\tau \approx 20$ fs and an intensity $I_h \approx 10^{14}$ W/cm^2. The Drude model yields the dielectric function of the plasma: $\epsilon(\omega) = 1 - (\omega_{pe}/\omega)^2/(1 + i\beta_e)$, where ω is the harmonic (angular)

frequency under consideration. $\omega_{pe} = (4\pi e^2 n_e/m_e)^{1/2}$ is the electron plasma frequency; e is the electron charge, m_e is the electron mass, $n_e = Zn_i$ denotes the electron number density as the product of average ionization Z degree and ion density n_i ($= 6 \times 10^{22}$ cm^{-3}). $\beta_e = \nu_e/\omega$ and the electron-ion collision rate is ν_e in the Spitzer approximation. As we are going to consider scattering of harmonic radiation, the nanorod should have a density above the critical one for this harmonic: $n_c = \omega^2 m_e/4\pi e^2$. Thus for example, for 10-th harmonic of laser wavelength $\lambda_L = 800$ nm one obtains $n_e > 1.4 \times 10^{23}$ cm^{-3} and therefore one should use $Z > 3$, which is easily achieved in the case of Carbon.

In the case of linear interaction, Mie theory can be used for the description of elastic electromagnetic wave scattering by arbitrary sized particles and beyond that, it allows the description of the electric and magnetic field distribution inside and outside the scattering object [18,19]. A main step is to solve the scalar Helmholtz Equation in an appropriate coordinate system and gain the vector solutions. For cylindrical scatters the solution of the scalar Helmholtz equation in this geometry can be written in the form of Bessel and Hankel functions of n-th order [19].

We do assume an incident plane wave, which is propagating along the x-axis and is polarized parallel to the y-axis, which can be written as: $\mathbf{E_y} = E_0 \exp(i\omega t - ikx)\mathbf{e_y}$, where $k = \omega/c$ and $\mathbf{e_y}$ is the unit vector in y direction. Now this wave can be expanded into a series via generalized Fourier expansion. When assuming an isotropic media the polarization is preserved and the internal and the scattered field are of a similar form. The scattered wave E_s has to be an outgoing one, which can be written in the following form [19]:

$$\mathbf{E_s} = E_0 \sum_{n=-\infty}^{\infty} (-i)^{n+1} A_n(ka, m)\mathbf{M_n}(\rho, \theta), \tag{1}$$

where n is the mode number of harmonics obtained via the transformation from Cartesian system to cylindrical one and $m = \sqrt{\epsilon(\omega)}$ is the refractive index of the target. The coefficient of vector harmonics have the form:

$$A_n(x, m) = \left[mJ'_n(x)J_n(mx) - J_n(x)J'_n(mx) \right] \left[mJ_n(mx)H_n'^{(1)}(x) - J'_n(mx)H_n^{(1)}(x) \right]^{-1}, \tag{2}$$

where J_n and H_n are the Bessel and Hankel functions respectively and the prime represents their spatial derivative. The vector function M_n has radial and azimuthal components as well:

$$\mathbf{M_n}(\rho, \theta) = \left[in(Z_n(\rho)/\rho)\mathbf{e_r} - Z'_n(\rho)\mathbf{e_\theta} \right] \exp(in\theta), \tag{3}$$

where $\rho = kr$ is the normalized spatial coordinate, e_r and e_θ are the unit vectors. Fields along the rod's axial direction are generated only in the case of S-polarization, which is not considered here. In the above expression Z_n is the generating function for the scattered fields which coincides with the Hankel function of the first kind, also used in Eq. (2).

In the case of cylindrical symmetry one can find that the amplitude of the scattered field is maximal for $m^2 = -1$ in the limit of very small rod radius ($ka \ll 1$), which immediately shows that in collision-less case the resonant density is single-valued: $n_e = 2n_c$ [19]. It can be easily found by expressing the Bessel functions with their asymptotic form, which leads to a simplified expression of the coefficients:

$$A_n(x \to 0, m) = \left(1 + i\frac{m^2 + 1}{m^2 - 1}\frac{C_n}{x^{2n}} \right)^{-1}, \tag{4}$$

where $C_n = (2^n n!)^2/(n\pi)$. For small object radius this approximated expression can be used instead of Eq. (2), however for $ka > 0.1$ this approximation is not valid any more, especially in the case of higher order modes.

The dependence of the scattering coefficient on electron density in the ionized nanorods is shown in Fig. 2 for two values of target radius. The first important thing to be noted here is that for larger rod radius the interval of resonance (width of the peak) is wider. This means that with a thicker rod a wider range of electron density value can be used to excite a cylindrical mode. It will be important in the case of higher order harmonics, for which ka is large. On the other hand from Fig. 2 it is apparent that for a non-ionized Carbon target the amplitude of the scattered radiation is much lower than in the ionized case. The value of the refractive index is taken from Ref. [12]. This is the main advantage of using the plasma phase in Mie scattering and the fact that Carbon ions with with charge state >3+ provide near-resonant electron density makes this material very attractive.
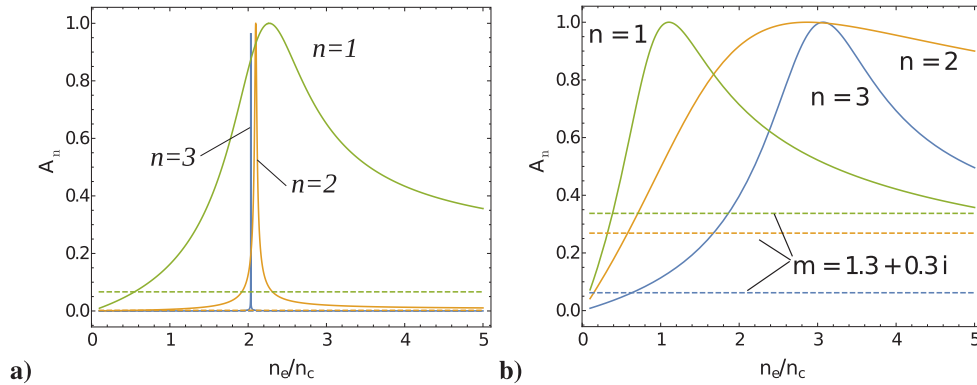
Fig. 2. Vector function coefficients used in Eq. (1) which define the amplitude of the scattered field for two normalized radius values: $ka = 0.5$ (a) and $ka = 2$ (b). The absolute value of the coefficient (A_n) is calculated by using Eq. (2) with purely imaginary refractive index (full lines) and with non-ionized graphite target (dashed line) for $n = 1$, $n = 2$ and $n = 3$.

The resonant density increases by increasing the nanorod radius, which is shown more clearly in Fig. 3, where the curves where obtained numerically by finding the maximum of Eq. (2). The optimal density (for which the A_n coefficient is maximum) gets higher in the case higher order modes. To obtain the resonant scattering of the harmonic with the wavelength $\lambda_9 = \lambda_L/9 = 89$ nm one should take the electron density to be $n_e \approx 3.5 \times 10^{23}$ cm^{-3} (C^{6+} for instance) in the case of $ka \approx 1$, but with larger normalized radius higher order modes can also be efficiently excited. For example with $ka = 2$ the second and third cylindrical mode of the 7th harmonic can be excited simultaneously if the target is ionized to C^{4+}, because in this case $Zn_i = n_e \approx 3n_c(\lambda_7)$. For the scattering of shorter wavelengths one should use different material, like Si which provides higher electron density at the same temperature.

Within the theory of Mie scattering it is known that the field amplitude on the target surface can be enhanced significantly. The high field amplitude in the near-field is expressed by the vector function M_n in Eq. (3). This is plotted in Fig. 3(b) as a function of radius. It shows that higher order modes have larger amplitude for small radius ($n = 2$), but in Fig. 2 it can be seen that this high amplitude is preserved for a narrow range of the refractive index. For example a nanorod with normalized radius of $ka = 0.03$ can amplify the local field by 100 times in the first mode and by 5000 times in the second mode. It means that the amplitude of modes with large n number is higher, but it requires very precise value of m (see Fig. 2(a)), or electron density. Such a strict constrain can be weakened by using thicker nanorods. However, for larger ka values the value of M_n at the target surface is not so high, therefore field amplification factor larger than 100 is practically not possible.
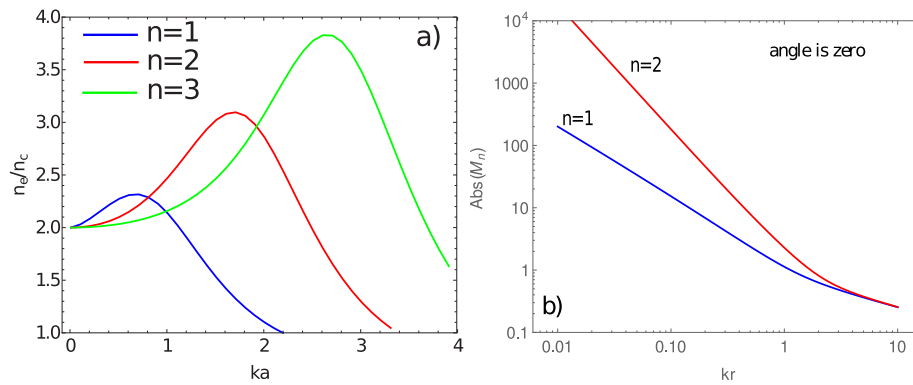
Fig. 3. (a) Normalized target density for which A_n ($\beta_e = 0$) is maximal versus the target radius for different mode numbers. (b) The absolute values of the vector harmonics are plotted (Eq. (3) with $\theta = 0$). At the rod surface the field enhancement corresponds to $r = a$ in this figure.

3. Particle-in-cell simulations

In our study we use the EPOCH 2D particle-in-cell code [?] for the investigation of the complex electron dynamics and light emission from the cylindrical finite size targets considered here. The typical oscillation amplitude of the electrons near the plasma surface for our parameters is about 0.5 nm, therefore these simulations require very high resolution and are computationally demanding. The used grid size in all simulations is always smaller than 1 nm, which ensures also the realistic representation of the circular boundaries even in the case of 20 nm thick nanorods. The plasma is represented by 200 particles in each cell occupied by the target.

3.1. Scattering of a single harmonic wave

Here we consider the interaction of a single frequency (9th harmonic) with infinitely long cylindrical object, which is a nano-rod. The field intensity is $I_h = 10^{13}$ W/cm^2. The spatial distribution of energy density is shown in Fig. 4, upper row, where the electron density is set according to the resonant modes indicated in the pictures and collisions are not included. The fields presented here are calculated by subtracting the field of the incoming planewave from the output of the simulation, which contains the incoming and scattered fields together. This simple method basically give us the fields emitted by the target electrons during the interaction.

In the lower row of Fig. 4 the results of analytical theory are shown, using the equations presented in the previous section, which are in good agreement with the simulations. Here mode numbers up to $n = 9$ are present and m is set to the resonant value of one selected mode. We have performed the same simulations with collisions switched on and the difference was negligible, which confirms that the relevant collision rates are much smaller than the harmonic frequency. The observed good agreement confirms that particle-in-cell simulation is a suitable tool to reproduce the Mie scattering in collision-less plasma (or in the case of low β_e parameters). It is worth to mention that within the laser focal spot size $d_L > a$, a plane wave is a good approximation.

The angular distribution of the scattered field is basically defined by the vector function M_n, which gives a very simple dependence on angle: the first mode is always symmetric (forward and backward emission is the same) and the angular distribution of higher order modes is defined by the mode number, i.e. the radiation in 2π is divided to $2n$ parts, each having different phase. It means that the non-symmetric scattering pattern is a consequence of the interference of different cylindrical modes excited at the target surface. The angular distribution can be manipulated by changing the density of the target, since each mode has a peak amplitude at different refractive
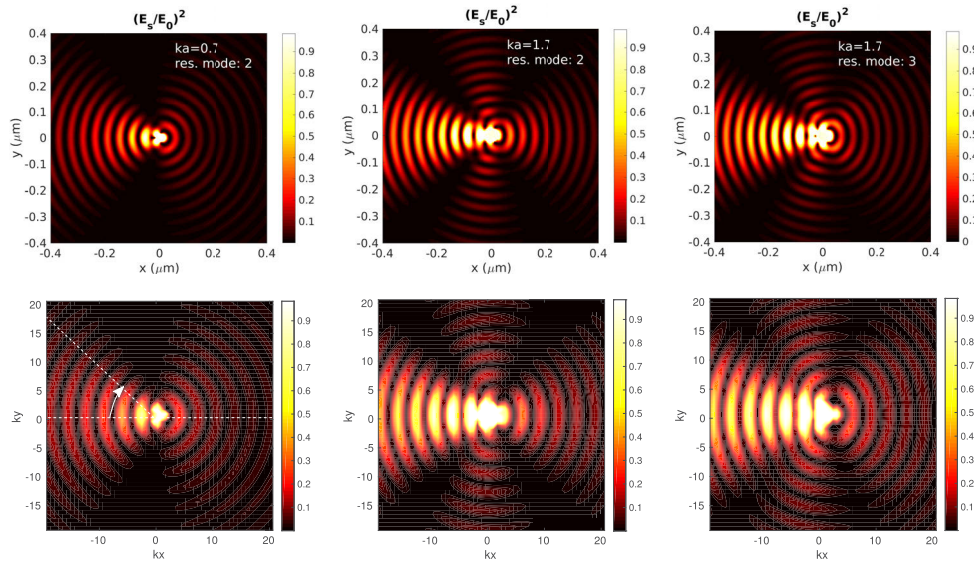
Fig. 4. 2D distribution of the scattered field (normalized to the incoming wave amplitude and only the 9th harmonic is present) from collision-less simulations (upper row) and from analyitical theory (lower row). The plane-wave propagates from right to the left and the white arrow shows the positive direction of θ angle.

index values. In Fig. 4, for $ka = 0.7$ the resonant densities of the first three modes are: $2.316n_c$, $2.206n_c$ and $2.068n_c$, while for $ka = 1.7$ these values are: $1.325n_c$, $3.096n_c$, $2.66n_c$ and for the forth mode $2.266n_c$.

The most intense radiation is expected at $\theta = 0$ (in the direction of the incoming wave), because at this angle (see Eq. (3)) the modes are in phase and positive interference occurs. However, if the density is set very precisely, close to the resonant values for the higher order modes, then scattering at larger angles can also be achieved. The interference of such components can result in complicated patterns, but at least 10 % of the radiation can be directed along a well defined angle. This is shown in Fig. 4 for two target radii and for different resonant densities.

In reality the resonance of a single mode is not possible to achieve as precisely as in the simulation. However, even if the electron density slightly changes in time the coefficient A remains close to one if the normalized radius is large enough, i.e. $ka>1$ (see Fig. 2). It is worth to mention that at $\theta = 90°$ the radiation is almost zero and most of the scattered radiation is emitted in forward and backward directions in a limited cone angle. This has an important consequence on the diffraction, because the scattered energy is not uniform, but most of the radiation will remain close to the incoming wave axis. In the following we set the electron density to a fixed value and investigate the effects of target properties.

The diffraction patterns obtained from simulations with many nanorods are presented in Fig. 5 for different nanorod thicknesses. The target is more realistic in this case because it consists of partially ionized Carbon (C^{4+}) and electrons at 200 eV temperature with realistic number density, which means $n_e = 2.4 \times 10^{23}$ cm^{-3} $\approx 6n_c(\lambda_5) \approx 3n_c(\lambda_7) \approx 1.7n_c(\lambda_9)$. The laser wavelength and peak intensity is the same as in Fig. 4, but here we consider Gaussian envelopes in the longitudinal and transverse directions. The separation between nanorods is the same in the x and y directions: $D_x = D_y = 3\lambda_9$ for the thicker nanorods and $D_x = D_y = 2\lambda_9$ for the thinner nanorods. In Fig. 5(a,c) the transmission is higher due to the small thickness of the rods, while the incoming radiation is scattered more efficiently in Fig. 5(b,d), where thicker nanorods are used. The transmission can be decreased by reducing the distance between nanorods or by increasing

their thickness. The angular distribution of the scattered wave is the same as in the case of a wave packet, which is presented in the next section.
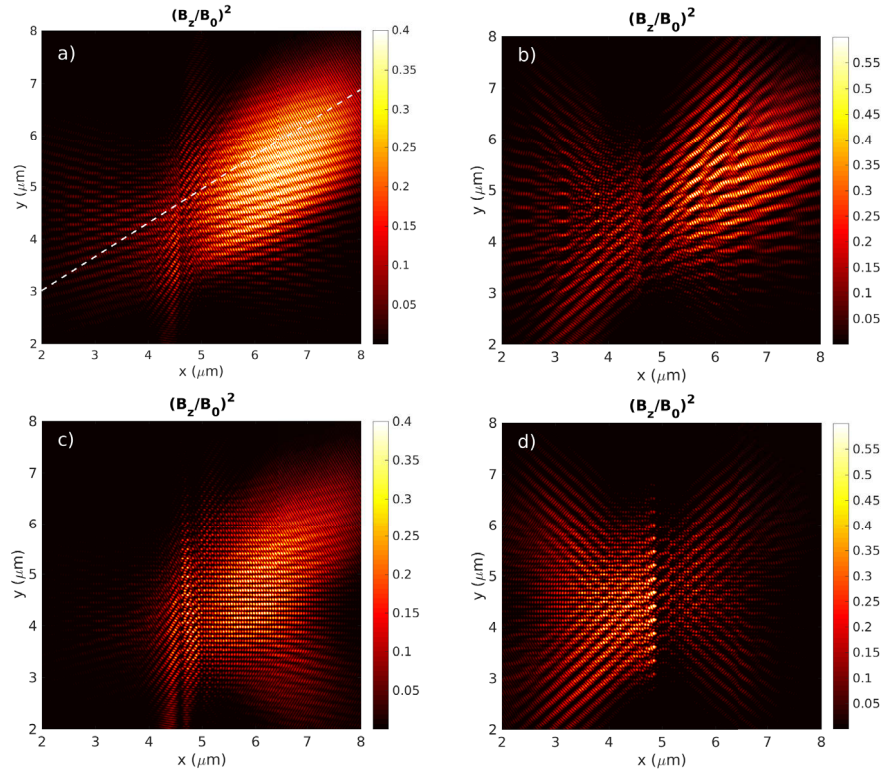

Fig. 5. Diffraction pattern of the normalized energy density for $a = 9$ nm (a,c) and for $a = 30$ nm (b,d) rod radius and for separation distance $D_x = D_y = 3\lambda_9$ in (b,d), while $D_x = D_y = 2\lambda_9$ in (a,c). The number of nanorod array columns is also varied: 1 in (a,b) and 3 in (c,d). The 15 fs long pulse propagates from the lower left corner towards the upper right corner and the white dashed line shows the axis of propagation. The incidence angle is $\theta_0 = 30°$.

3.2. Scattering of wave packet

First let us consider the scattering by a single nanorod. The harmonic radiation consists of many frequencies with well defined phases, which depends on the nature of the emitting medium. Here from the third up to the 15th harmonics are included, thus the nanorods interact with a train of attopulses. Now for each harmonic scattering conditions will be different, because the normalized quantities define the scattered field pattern.

In the case of many wavelengths it is better to analyse the scattered field in the frequency domain by applying the Fourier transformation. The results are presented in Fig. 6 for two values of normalized rod radius. One can see that in the case of thinner rod the 9th and 7th harmonics are scattered more efficiently (Fig. 6(a)), because for this frequency the dimensionless quantity n_e/n_c is still in the range of resonance, as it is shown in Fig. 2(a). For longer wavelengths the normalized density gets higher, but the coefficient of the first mode decays slowly with increasing density which allows for efficient scattering. For larger radius the higher order modes also appear with significant amplitude, which is seen in Fig. 6(b). This can be explained by the wide peaks of

A_n shown in Fig. 2(b). The maximum value of A_1 is shifted towards lower normalized densities (see Fig. 3(a)) which also leads to stronger scattering of higher harmonics.
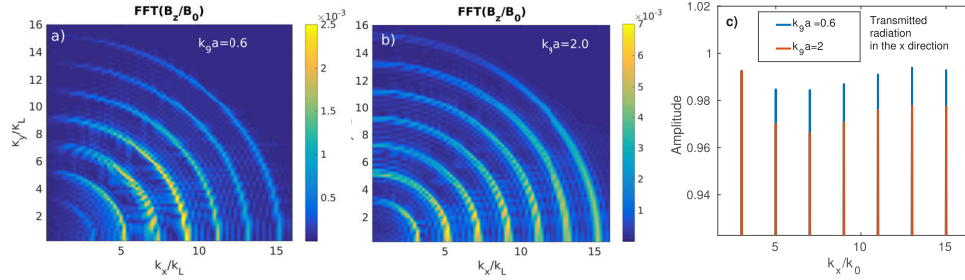
Fig. 6. Distribution of the scattered radiation in the Fourier space for two different values of radius: $a = 9$ nm (a) and $a = 30$ nm (b). The change in the amplitudes of the harmonics is also shown (c).

It is important to distinguish between scattered and absorbed energy. Via the electron oscillations induced during the interactions the ions are slightly accelerated by the charge separation field, in this way the field energy is absorbed. The surface field amplitude is stronger for smaller ka, which means that the absorption, and the reduction in amplitude, is more pronounced in the case of the 7th harmonic. The electron density is closer to the resonance of the 9th harmonic which also loses energy via scattering at large angles. This is confirmed in Fig. 6(c), where the transmitted (going in the x direction or at $\theta = 0°$) normalized energy density values are shown for all frequencies. In general for absorption the thinner nanorods while for scattering the thicker nanorods are more appropriate as long as the electron density is close to the resonant one.

When more nanorods are used the interference between scattered waves start to play an important role. From Fig. 5 it is difficult to identify the angles of scattered light, but in the Fourier space it is possible to extract well defined angles. The intensity distribution of the scattered radiation in the (k_x, k_y) space is shown in Fig. 7, where along the dashed circular line we can find the intensity distribution of the 9th harmonic. One important feature of the scattering for these parameters is that the signal in the specular direction ($\theta = 150°$) is very weak. Instead there is strong backward reflection. The transmission is strong in all cases except the case of thicker rods with 3 array arrangement, as it is seen in Fig. 5(d) as well.

The spectral distribution of the transmitted radiation in the original direction of the laser pulse is shown in Fig. 8. The trivial output of the scattering is visible here as well: the higher number and larger radius of nanorods reduces the intensity of transmitted waves. The outcome of these results is in agreement also with 6 where the 7th harmonic is absorbed the most efficiently. In the case of the 5th harmonic the parameter ka is even smaller, but the ratio n_e/n_c is far from the resonant value.

The angular distribution of transmitted fields after scattering can be understood by the von Laue formula which states the condition for constructive interference: $\mathbf{D} \cdot (\mathbf{k} - \mathbf{k}') = 2\pi N$, where $\mathbf{D}$ is the vector connecting two neighboring nanorods and $\mathbf{k}$, $\mathbf{k}'$ are the incoming and reflected wave number vectors, respectively, and N is an integer, also called as the order of interference. The angles with respect to $\mathbf{k_x}$, where positive interference can be expected in the transmitted radiation, are then expressed with the following formula:
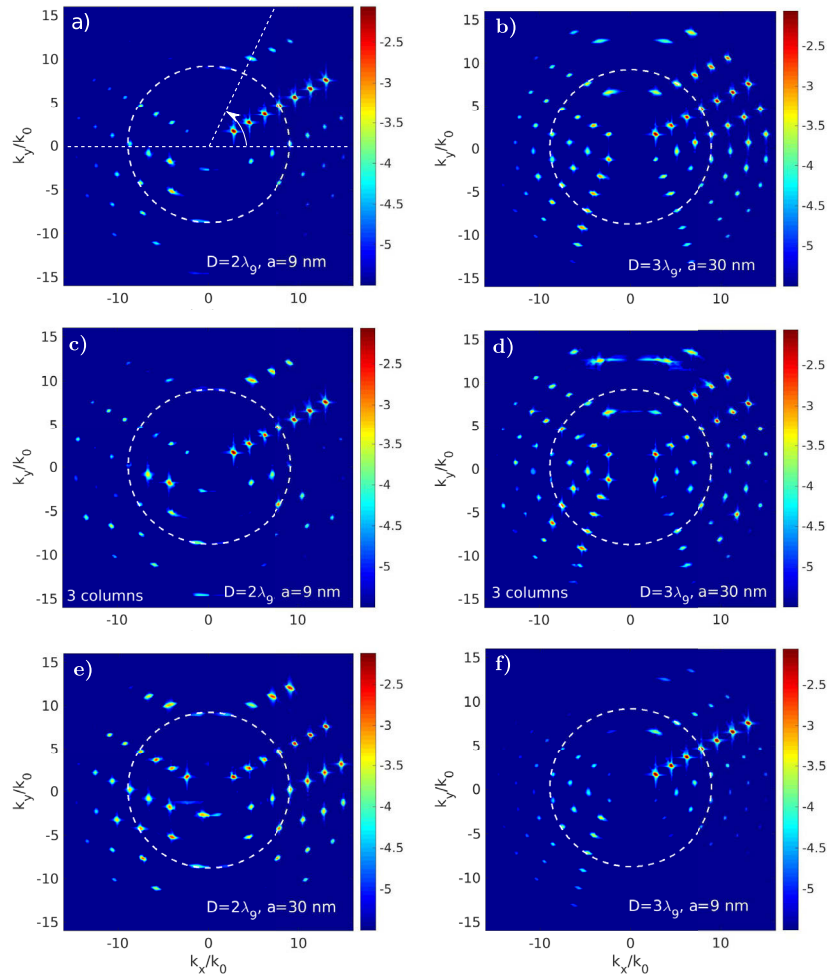
$$\theta_t = \arcsin(sin(\theta_0) - N\lambda_h/D) \tag{5}$$

and for the reflected radiation:

$$\theta_r = \pi - \arcsin(sin(\theta_0) - N\lambda_h/D). \tag{6}$$

In the case of a single rod array there is only one orientation in the y direction, which is shifted
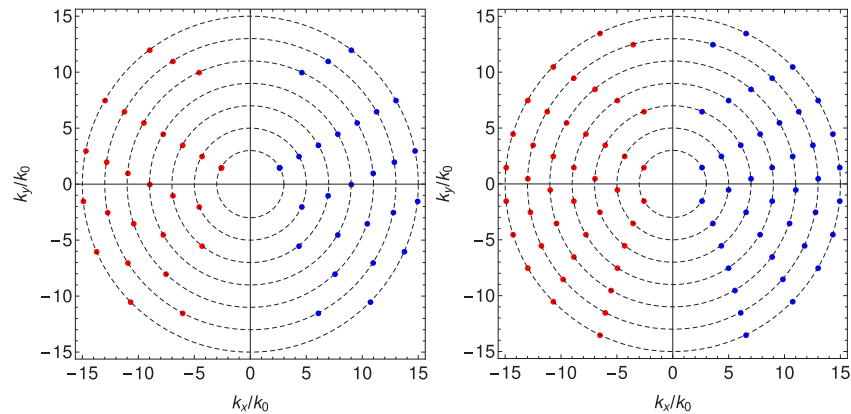
Fig. 7. (a,b,c,d) Intensity distribution from simulation in the *k* space corresponding to the same simulations as Fig. 5, but with multiple harmonic frequencies. The white arrow shows the direction in which the θ angle is measured. (e,f) Additional simulations showing that changing the rod thickness does not affect the scattered field pattern, only the scattered intensity. In all pictures the color code represents $log_{10}[|FFT(B_z/B_0)|^2]$.
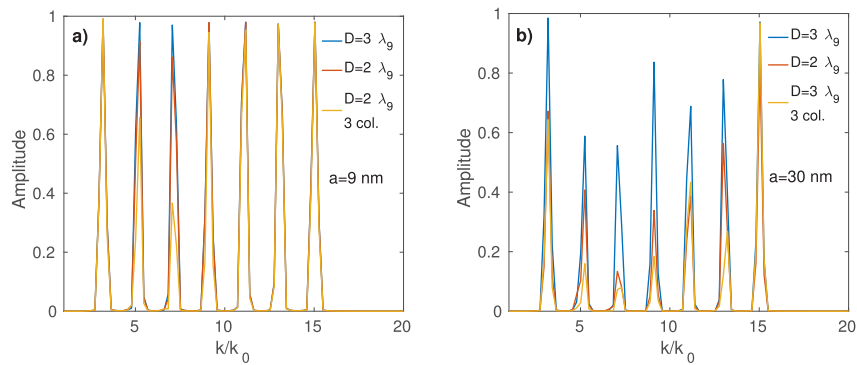

Fig. 8. Spectral intensity distribution of transmitted radiation in the direction of the incident pulse ($\theta_t = 30°$, $N = 0$).

by 90° with respect to the $\mathbf{k_x}$ axis. In the case of $D = 2\lambda$ by using Eq. (5) one can easily obtain the angles corresponding to the red dots along the dashed line in Fig. 7(a). Beside the zero order diffraction (30°) there is radiation propagating in the 0° and 90° directions, corresponding to $N = 1$ and $N = -1$. The negative first order is not well visible in our simulation, because the forward scattering by a single harmonic is limited in angle to ±40° (See Fig. 4). For larger D value (see Fig. 7(b)) additional angles also appear which are $\theta_t = 9.6°$ and $\theta_t = 56.4°$ according to Eq. (5) and several other negative angles corresponding to higher order diffraction.

In the case of multiple frequencies the scattering angles are also predictable by Eqs. (5) and (6), only the wavelength has to be replaced with the harmonics wavelengths. One important consequence of the shorter wavelengths is the increase of the order of diffraction (N) visible in the scattered light, because $N_{max} \sim D/\lambda_h$, according to the diffraction theory. With other

Fig. 9. Intensity distribution from theory in the k space corresponding to $D = 2\lambda_9$ (left) and $D = 3\lambda_9$ (right). The blue dots are calculated by Eq. (5) and the red dots by Eq. (6). All parameters are the same as in Fig. 7.
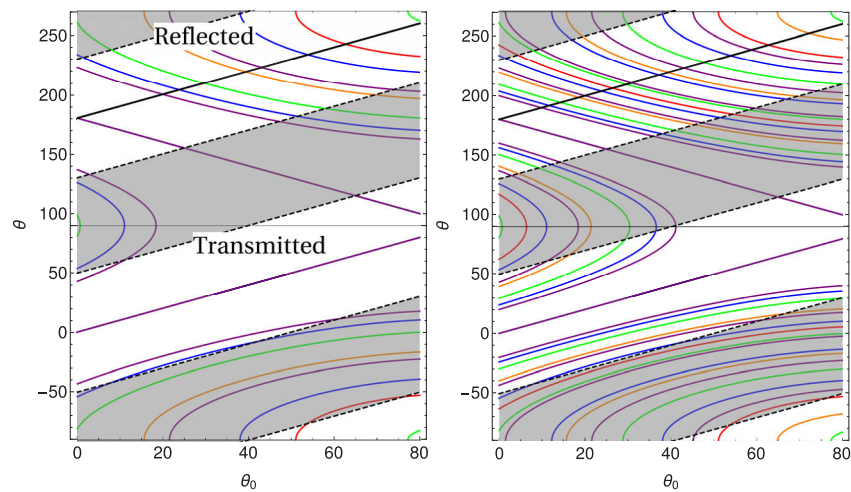
Fig. 10. Theoretical prediction for the angular distribution of the transmitted and reflected harmonics as a function of incidence angle for two configurations: $D = 90$ nm (left) and $D = 180$ nm (right). The shaded areas indicate the regions where low intensity radiation is expected. The colors correspond to harmonic numbers: $h = 5$ (red), $h = 7$ (orange), $h = 9$ (green), $h = 11$ (blue), $h = 13$ (purple).

words the angle difference between diffraction orders becomes less: $\sim \arcsin(\lambda_h/D)$ [18]. The intensity distributions of scattered light in the Fourier space are very similar for 1 (Fig. 7(a,b)) and for 3 (Fig. 7(c,d)) nanorod arrays, therefore the size of our nano-forest target does not modify significantly the scattering. More important is the distance between the nanorods.

The results of Eqs. (5) and (6) are shown in Fig. 9, which are in perfect agreement with the simulations. Having a reliable theory we can perform a parameter-scan over different incidence angles and for different distances between the nanorods. Two examples are shown in Fig. 10, where the gray areas indicate the angles where the scattered light intensity is low. This is a consequence of the P-polarization and it has been shown in Fig. 4, where the scattered light is expected in the forward and backward direction within a half cone angle of $\approx 50°$.

4. Waveform synthesis of XUV pulses

The change in the waveforms at different angles has been already illustrated in Fig. 1, which now can be understood by the applied theory. In Fig. 10 we can see the difference between the transmitted and reflected (in the direction opposite of the laser propagation indicated by the black line) radiation. In the forward direction higher frequencies are scattered, while in the backward mostly lower frequencies appear. If the value of D is small enough (here $D = 90$ nm in Fig. 10) the scattering of transmitted radiation can be fully eliminated and high-order harmonics can be transported at $\theta_r = 200°$ for a wide range of incidence angles. The scattered radiation is more rich in frequencies at smaller incidence angles and in the case of larger D values. In principle it is possible to obtain the expected angle of one or several harmonics for any value of θ_0.

In principle the spectrum of the scattered radiation at a desired angle can be manipulated by tuning the rod radius or ionization level in the target. The amplitude of the far-field is defined by the function $A_n(ka, \sqrt{1 - n_e/n_c})$. For each harmonic, which can be found at a given θ angle (according to Eqs. (5) and (6)) the total amplitude can be calculated using Eq. (1). The intensity obtained in this way us further modulated by the intensity function used in the diffraction theory [18] and in the far-field the following expression can be given for the scattered harmonic intensity:

$$I_h^s = \left[\frac{\sin(k_h D p/2)}{k_h D p/2} \right]^2 \left[\sum_n A_n(k_h a, m_h) \cos(n\theta_{t(r)} - n\theta_0 + n\pi/2) \right]^2, \tag{7}$$

where $p = \sin(\theta_{t(r)}) - \sin(\theta_0)$, $k_h = 2\pi/\lambda_h$ and $m_h = \sqrt{1 - n_e/n_c(\lambda_h)}$. Due to the different values of ka and n_e/n_c each harmonics will have different amplitudes, which now can be calculated. The first term in the right hand side of Eq. (7) defines the angular interval of intense scattering and the maximum order of diffraction. This effect can be seen also in Fig. 7, where N_{max} is increasing with the harmonic order. It can be seen that two or more harmonic frequencies can propagate at nearly the same angle and they may overlap. In this way the XUV pulse synthesis is possible for harmonics with characteristics curves laying very close to each other in the angle-diagram, shown in Fig. 10.

5. Conclusion

Ionized nanorod (or nanowire) arrays with periodic structures are found to be suitable scattering devices in the XUV regime. When the ionization level is such that the electron density in the target is close to the resonant density the scattering and extinction efficiency increases and reaches the few percent level in the case of a single nanorod. In the case of multiple nanorods the efficiency increases linearly with the number of nanorods and the energy scattered in a given direction can reach the level of 10s percents of the incoming radiation energy. The scattering pattern generated with a well-defined two-dimensional array is well described by the classical Laue formula. We chose C^{4+} as target material and prove the flexibility and simplicity of such diffraction devices with the help of Particle-in-Cell simulations.

Beside efficient scattering of selected wavelengths at selected angles the nanorod array proposed here behaves as a filtering device in the direction of the incident laser pulse. One harmonic frequency can be completely removed from the incoming radiation and the intensity of nearby harmonics is also reduced during transmission. The frequency which is filtered out can be chosen by tuning the electron density in the target or by changing the target material.

Disclosures

The authors declare no conflicts of interest.

References

1. T. Fennel, K.-H. Meiwes-Broer, J. Tiggesbäumker, P.-G. Reinhard, P. M. Dinh, and E. Suraud, "Laser-driven nonlinear cluster dynamics," Rev. Mod. Phys. **82**(2), 1793–1842 (2010).
2. S. X. Hu and Z. Z. Xu, "Enhanced harmonic emission from ionized clusters in intense laser pulses," Appl. Phys. Lett. **71**(18), 2605–2607 (1997).
3. T. V. Liseykina, S. Pirner, and D. Bauer, "Relativistic attosecond electron bunches from laser-illuminated droplets," Phys. Rev. Lett. **104**(9), 095002 (2010).
4. U. Teubner and P. Gibbon, "High-order harmonics from laser-irradiated plasma surfaces," Rev. Mod. Phys. **81**(2), 445–479 (2009).
5. B. Dromey, M. Zepf, A. Gopal, K. Lancaster, M. S. Wei, K. Krushelnick, M. Tatarakis, N. Vakakis, S. Moustaizis, R. Kodama, M. Tampo, C. Stoeckl, R. Clarke, H. Habara, D. Neely, S. Karsch, and P. Norreys, "High harmonic generation in the relativistic limit," Nat. Phys. **2**(7), 456–459 (2006).
6. G. D. Tsakiris, K. Eidmann, J. M. ter Vehn, and F. Krausz, "Route to intense single attosecond pulses," New J. Phys. **8**, 19 (2006).
7. M. F. Ciappina, J. A. Pérez-Hernández, A. S. Landsman, W. A. Okell, S. Zherebtsov, B. Förg, J. Schötz, L. Seiffert, T. Fennel, T. Shaaran, T. Zimmermann, A. Chacón, R. Guichard, A. Zaír, J. W. G. Tisch, J. P. Marangos, T. Witting, A. Braun, S. A. Maier, L. Roso, M. Krüger, P. Hommelhoff, M. F. Kling, F. Krausz, and M. Lewenstein, "Attosecond physics at the nanoscale," Rep. Prog. Phys. **80**(5), 054401 (2017).
8. S. Jiang, L. L. Ji, H. Audesirk, K. M. George, J. Snyder, A. Krygier, P. Poole, C. Willis, R. Daskalova, E. Chowdhury, N. S. Lewis, D. W. Schumacher, A. Pukhov, R. R. Freeman, and K. U. Akli, "Microengineering laser plasma interactions at relativistic intensities," Phys. Rev. Lett. **116**(8), 085002 (2016).
9. P. Balcou, R. Haroutunian, S. Sebban, G. Grillon, A. Rousse, G. Mullot, J.-P. Chambaret, G. Rey, A. Antonetti, D. Hulin, L. Roos, D. Descamps, M. Gaarde, A. L'Huillier, E. Constant, E. Mevel, D. von der Linde, A. Orisch, A. Tarasevitch, U. Teubner, D. Klöpfel, and W. Theobald, "High-order-harmonic generation: towards laser-induced phase-matching control and relativistic effects," Appl. Phys. B **74**(6), 509–515 (2002).
10. A. L'Huillier and P. Balcou, "High-order harmonic generation in rare gases with a 1-ps 1053-nm laser," Phys. Rev. Lett. **70**(6), 774–777 (1993).
11. V. T. Platonenko and V. V. Strelkov, "Generation of high-order harmonics in a high-intensity laser radiation field," Quantum Electron. **28**(7), 564–583 (1998).
12. A. B. Djurisic and E. H. Li, "Optical properties of graphite," J. Appl. Phys. **85**(10), 7404–7410 (1999).
13. J. Joannopoulos, R. Meade, and J. Winn, *Photonic Crystals* (Princeton University Press, 1995).
14. X. Lin, X. Zhang, K. Yao, and X. Jiang, "Wide-range and tunable diffraction management using 2d rectangular lattice photonic crystals," J. Opt. Soc. Am. B **31**(5), 1145–1149 (2014).
15. B. W. Batterman and H. Cole, "Dynamical diffraction of x rays by perfect crystals," Rev. Mod. Phys. **36**(3), 681–717 (1964).
16. L. Drescher, O. Kornilov, T. Witting, G. Reitsma, N. Monserud, A. Rouzée, J. Mikosch, M. J. J. Vrakking, and B. Schütte, "Extreme-ultraviolet refractive optics," Nature **564**(7734), 91–94 (2018).
17. A. V. Baez, "A self-supporting metal fresnel zone-plate to focus extreme ultra-violet and soft x-rays," Nature **186**(4729), 958 (1960).
18. E. W. M. Born and, *Principles of Optics* (Pergamon Press, 1959).
19. C. F. Bohren and D. R. Huffman, *Absorption and Scattering of Light by Small Particles* (Wiley, 1998).